Imaging and detection of cracks in metallic structures with Eddy current sensors

Dominique Placko
SATIE, ENS Cachan, CNRS,
61 avenue du président Wilson
94 235 Cachan Cedex
+33 (0) 1 47 40 55 81
dominique.placko@satie.ens-cachan.fr

Thierry Bore
Université Paris Est, IFSTTAR
58, boulevard Lefebvre
75732 Paris Cedex 15
Present address : Andra
1-7, rue Jean-Monnet - 92298
Châtenay-Malabry cedex
thierry.bore@andra.fr

Pierre - Yves Joubert
SATIE, ENS Cachan, CNRS,
61 avenue du président Wilson
94 235 Cachan Cedex
+33 (0) 1 47 40 55 90
pierre-yves.joubert@satie.ens-cachan.fr

ABSTRACT
In this paper we will focus on the modeling of electromagnetic (EM) systems, in the aim of using it in an inversion scheme. The purpose will consists in imaging cracks with eddy current sensors, through an estimation of the conductivity of the piece of metal under test. There are plenty of industrial applications in Non Destructive Evaluations for monitoring of cracks in structures used in Aeronautics, Metallurgy, ships building and so on. For modeling, a relatively new developed technique, called 'Distributed Points Source Method' (DPSM) has been used.

Keywords
Eddy currents, DPSM modeling, multi-frequency imaging

1. INTRODUCTION
Among different available techniques, such as X-ray, Gamma ray and thermal imaging to name a few, the eddy current non-destructive testing (EC NDT) technique remains a popular method of choice, when electrically conductive materials have to be tested. EC NDT has many advantages: it usually has a good reliability; it is a low cost and easy to use technique. An EC automatic testing process can be quick and efficient. EC NDT is based on the Faraday's induction law, that eddy currents are generated in an electrically conductive material as soon as the material is placed in a time varying magnetic field.

In order to achieve a realistic and reliable imaging technique, the first step consists to build an instrument that is capable of creating eddy currents in a given direction θ_i and at a given frequency f in the material under inspection. Then, the map of the magnetic perturbation field, due to the presence of the crack, is measured at the surface by an electromagnetic sensor. This is a dual problem: it is necessary to have an inducer able to provide a significant lighting of the object under test, when the sensor must deliver an accurate map of the surface electromagnetic field. This is the reason why generally, the coil used for inducing the eddy currents is not used for the detection, but an array of micro-detectors is preferably used for field mapping. Such measurement arrays are generally preferred to single sensor probes for the sake of spatial resolution, acquisition speed and sensitivity [1,2,3]. In this context, magneto-optical imaging systems [4,5] have good prospects to fulfill EC NDT inspection rapidity, provided the inspected structure is planar. To that purposes, an original EC imaging device was developed in [6] and presented in [7, 8]. The device uses an inducer able to generate a uniformly oriented EC with th material, and a linear magneto optical imaging film [7] which actually translates the surface magnetic map into light intensity, detected through an optical setp up and a CCD camera in a stroboscopic framework. The device presented in [8] allows magnetic maps of high sensitivity and spatial resolution (100 µm ×100 µm) to be measured over a large planar inspection area (65 mm diameter disc), without scanning operation and within a short time (in the order of a few seconds). Such an imaging device is particularly well suited to the quantitative imaging of cracks, provided that the EC/defects interactions can be accurately modeled, and that this model can be efficiently inverted. In what follows, the authors propose to use an original DPSM modeling, and to carry out the inversion of EC data to characterize cracks in the context of EC imaging.

NCMIP 2011, May 25, Paris, France

DOI 10.4108/icst.valuetools.2011.245817

2. D.P.S.M. MODELLING
2.1 Introduction
DPSM modeling was initially developed at ENS Cachan by Dominique Placko and his associates [9] since 2000, for solving electromagnetic and electrostatic 3D problems. This method was then extended to solve ultrasonic problems, in collaboration with Kundu and his associates, at the University of Arizona [10,11,12]. The basic principle of DPSM consists to substitute the actual source density which may exists in a given volume (due to eddy currents for example), for some arrays of Equivalent Sources Densities (ESD) also placed inside this object, near the boundary. The purpose consists to obtain the same values of the field radiated outside this object by the true values of sources than with the Equivalent Sources Densities. Simpler ESD can be point sources, for which radiating effect can be easily computed using singular Green's functions. Finite sources, interfaces and boundaries are modeled by distributions of such ESD. The final product of this approach is a semi analytical solution technique, which can be used for solving direct or inverses problems for generating the field pattern or producing images of internal defects.

2.2 DPSM formalism in Electromagnetic
This part explains the DPSM formulation in EM where elemental sources are small current vectors. For these particular sources, the electromagnetic field radiated can be computed with the Green functions, introduced without heavy approximations. So this modeling will be able to work accurately in a wide range of frequencies, and for a wide range of physical properties of the materials (conductivity, electrical permittivity, and magnetic permeability). When the problem is solved, all the elemental values of the sources are known, allowing the possibility to

compute fields and potentials in all the media of the problem. The initial formulation used to solve the equations is based on the calculation of the magnetic vector potential $\vec{A}_M$, including an important step which is the matching of the boundary conditions at the interfaces between different media. In a second step, electric and magnetic fields are derived from it and can be computed in the entire problem.

3. INVERSION SCHEME

3.1 Presentation of the direct formulation problem

The basic imaging process required the knowledge of a direct model, which can be used afterwards in an inversion scheme. It is well known that the raw inversion of a direct model is not possible because of the effect of noise: the smaller Eigen values of the direct matrix lead after inversion to a drastic amplification of noise, mainly which is out of the system bandwidth. To overcome this problem, it is possible to introduce a regularization, and we keep in this study a Wiener regularization, resulting from Gaussian assumptions on signals and noise, in a Bayesian context.

The main idea consists to introduce a global transfer matrix *M* between a set of *P* observations, placed in a vector *S* and a set of *N* parameters, placed in a vector *A*. The parameter vector *A* is representative of the contrast function of a given number of elemental volumes (called voxels) resulting from the sampling of the volume under test according to a pre-determinate mesh grid.

Let us write the relationship between the observation vector *S* and the parameter vector *A* in the following manner. In a first step, let us introduce a matrix $M_{\theta_i f_1}$ which is defined only for a given orientation θ_i of the inducers and a given frequency f_q of the driving currents:

$$S = M_{\theta_i fq}.A \Leftrightarrow S = \begin{pmatrix} m_{11} & m_{12} & m_{13} & \cdots & m_{1N} \\ m_{21} & m_{22} & m_{23} & \cdots & m_{2N} \\ m_{31} & m_{32} & m_{33} & \cdots & m_{3N} \\ \vdots & \vdots & \vdots & & \vdots \\ m_{P1} & m_{P2} & m_{P3} & \cdots & m_{PN} \end{pmatrix} . \begin{pmatrix} a(1) \\ a(2) \\ a(3) \\ \vdots \\ a(N) \end{pmatrix} \quad (1)$$

The purpose being crack imaging, let us consider that the specimen under inspection is a homogeneous material of conductivity σ_0, in which some defects or cracks may occur ($\sigma \neq \sigma_0$). Therefore, we can define the relative conductivity for each voxel :

$$a(n) = \frac{\sigma_0 - \sigma(n)}{\sigma_0} \quad (2)$$

We can see that for a voxel having a conductivity equal to *0* , $a(n)$ will be equal to *1*, and for a voxel having a conductivity equal to σ_0, $a(n)$ will be equal to *0*.

So, in order to identify all the terms of the matrix $M_{\theta_i fq}$, it is easy to compute the observation image S corresponding to a given location of a 'perturbation voxel' (which is only the one, among the totality of voxel, to have a different conductivity). For example, by taking $\sigma(n) = 0$ for the identification voxel (which corresponds to $a(n) = 1$), and $\sigma(k \neq n) = \sigma_0$ for all other voxels (which corresponds to $a(k \neq n) = 0$).

For example, if we assume that the voxel number *3* is the identification voxel, one gets:

$$S = M_{\theta_i fq}.A \Leftrightarrow S = \begin{pmatrix} m_{11} & m_{12} & m_{13} & \cdots & m_{1N} \\ m_{21} & m_{22} & m_{23} & \cdots & m_{2N} \\ m_{31} & m_{32} & m_{33} & \cdots & m_{3N} \\ \vdots & \vdots & \vdots & & \vdots \\ m_{P1} & m_{P2} & m_{P3} & \cdots & m_{PN} \end{pmatrix} . \begin{pmatrix} a(1) = 0 \\ a(2) = 0 \\ a(3) = 1 \\ \vdots \\ a(N) = 0 \end{pmatrix} \quad (3)$$

In this case, we can easily find the third column of $M_{\theta_i f_q}$:

$$S = M_{\theta_i fq}.A \Leftrightarrow S = \begin{pmatrix} m_{13} \\ m_{23} \\ m_{33} \\ \vdots \\ m_{P3} \end{pmatrix} \quad (4)$$

By moving the perturbation voxel from position *1* to the last position (*N*) one can see that all terms of the matrix can be determined.

To obtain a reliable estimate of all unknown parameters (included in vector *A*), we propose to compute different sub matrices corresponding to different conditions of excitation (as frequency and orientation change). Then, we perform some simulations corresponding to these different cases. In the case we have *n* different frequencies and *m* layers of voxel (each layer is located at z_i depth) the matrix M_{θ_i} obtained with the exciting current in direction θ_i, can be written in the following form:

$$M_{\theta_i} = \begin{pmatrix} M_{\theta_i f_1} \\ M_{\theta_i f_2} \\ \vdots \\ M_{\theta_i f_Q} \end{pmatrix} = \begin{pmatrix} M_{f_1 z_1} & M_{f_1 z_2} & \cdots & M_{f_1 z_m} \\ M_{f_2 z_1} & M_{f_2 z_2} & \cdots & M_{f_2 z_m} \\ \vdots & \vdots & & \vdots \\ M_{f_Q z_1} & M_{f_Q z_2} & \cdots & M_{f_Q z_m} \end{pmatrix} \quad (5)$$

The $M_{f_i z_i}$ matrix corresponds to those obtained when the defects are located in the j^{th} layer and for the q^{th} frequency. Its size obviously depends on the number of voxels of the observation image and the number of voxels chosen in the initial 3D volume mesh.

Afterwards, the global matrix is computed using different incident angles θ_i. If we have *R* different angles, the global matrix *M* will have the following expression:

$$M = \begin{pmatrix} M_{\theta_1} \\ M_{\theta_2} \\ \vdots \\ M_{\theta_R} \end{pmatrix} \quad and: \quad OBS = M.A \tag{6}$$

The global observation vector *OBS* contains all the elemental observations *S* respectively obtained for all couples of θ_i and f_q.

3.2 Identification of matrix *M* in the case of Eddy current tomography

The excitation device is composed of two rectangular inducers (with a length of *14 mm* and a width of *2 mm*) in order to create an excitation current as constant as possible in intensity and direction in the inspected area. The elemental identification defect is moved in the zone between the two coils. The Figure 1 illustrates the configuration of the two coils (oriented at θ =*0°*) and the displacement of the perturbation voxel in a cubing mesh. For the material, we choose $\sigma_0 = 17 \times 10^6 S$, corresponding to Inconel.

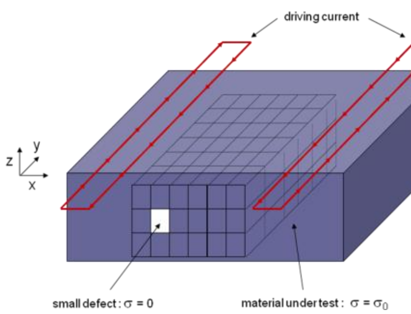

Figure 1 – Illustration of the displacement of the perturbation voxel

The configuration of the problem geometry is sketched in Figure 2. It has *m=3* layers of *11* by *11* voxels (that means a total number of *N=363* voxels). We choose to use a perturbation voxel of spherical geometry, instead of a cubic one, to make sure that all normal vectors associated with the test points meshed at the surface of this element, are uniformly distributed in the whole space. Radius of this spherical object is equal to R_s*=0.6 mm*.

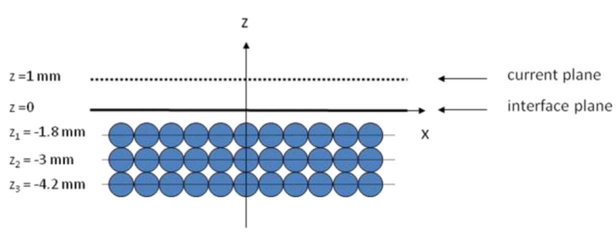

Figure 2 – Geometry of the problem in the xOz plane

The value of excitation frequency can be chosen to take into account the material properties (electrical conductivity and permeability). We choose to use three different frequencies:

f_1 *=3600 Hz*, f_2 *= 1600 Hz* and f_3 *=900 Hz*. These frequencies are chosen to obtain skin depth (with corresponding to the magnetic) effects in the range of the depth inspected (from 1.8 mm up to 4.2 mm). The skin depth δ is defined as $\delta = 1/\sqrt{\pi\mu\sigma_0}$ with μ the permeability of the material.

The observation vector *S* is made of all values of the magnetic field observed at the surface. In the application described here, the map of measurement has a size of *30 mm x 30* mm and is *40* by *40* pixels, giving a total number of *P=40x40 =1600* measurement points for the normal component (H_z) of the magnetic field. Only the normal component of the magnetic field is measured by our Imager, and then only this component is kept here in our theoretical approach. Calculations are carried out for *R=3* different orientations of the driving current: θ *=0°*, *45°* and *90°*.

The series of images in Figure 3 shows a top view of the real part of the magnetic field at the surface and are calculated with a defect in the middle of the displacement area. The figure 3.a was calculated with a coil oriented at θ *=0°* and with a defect at a depth of z_1 and a frequency equal to f_1. The figure 3.b was computed with the same frequency and depth but with a coil oriented at θ *=45°*. The figure 3.c was computed with coil oriented at θ *=0°* and with a defect at a depth of z_2 and a frequency equal to f_3. The figure 3.d was computed with coil oriented at θ *=90°* and with a defect at a depth of z_3 and a frequency equal to f_2.

We may notice that since we use *3* layers of *121* voxels at *3* frequencies, for building the complete matrix (for only one position θ_i of the inducers) we need to compute *121x3 x3=1089* images. The general case presented by equation 5 then becomes:

$$M_{\theta_i} = \begin{pmatrix} M_{f_1 z_1} & M_{f_1 z_2} & M_{f_1 z_3} \\ M_{f_2 z_1} & M_{f_2 z_2} & M_{f_2 z_3} \\ M_{f_3 z_1} & M_{f_3 z_2} & M_{f_3 z_3} \end{pmatrix} \tag{7}$$

This operation is realized with three different orientations of currents; then the global tomography matrix can be written as:

$$M = \begin{pmatrix} M_{\theta_0} \\ M_{\theta_{45}} \\ M_{\theta_{90}} \end{pmatrix} \tag{8}$$

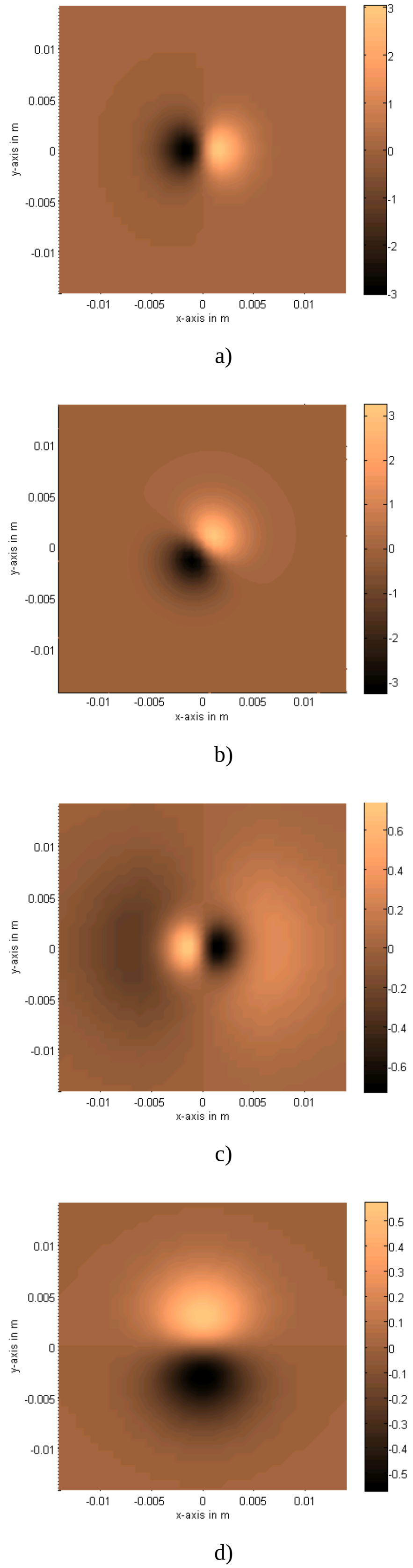

Figure 3 – Examples of images used in the computation of the tomography matrix

4. RESULTS IN CRACKS IMAGING

4.1 Test of the inversion process

First, let us build some images using the model and then invert it. This step shows that the direct multi-frequency modeling matrix is easily invertible. The inversion formulation is obtained simply by a least mean square formulation, and gives an estimation of *A*, called $\tilde{A}$:

$$\tilde{A} = [(M^t.M)^{-1}.M^t].OBS \qquad (9)$$

We present here an example with an 'L' shaped crack. The images contained in the *OBS* vector are obtained by assembling some elemental voxels. The figure 4 represents some images (only the real parts of the images are shown). The figure 4.a was computed for a coil oriented at $\theta = 0°$ and a frequency equal to f_2, the figure 4.b was computed for a coil oriented at $\theta = 45°$ and a frequency equal to f_2, the figure 4.c was computed for a coil oriented at $\theta = 45°$ and a frequency equal to f_3 and the figure 4.d was computed for a coil oriented at $\theta = 90°$ and a frequency equal to f_3.

The inversion results are presented on figure 5, showing different relative values of conductivity in layers 1, 2, and 3. The inversion results show that without noise, the estimated vector $\tilde{A}$ is identical to the current vector A. The top picture shows the lexical values of $\tilde{A}$, then the bottom figure represents it in 3D view.

Please remember that $\tilde{A}$ (or A) represents the relative variation of conductivity (equation 2). If $a(n) = 1$, the conductivity falls to *0* (like for a crack), and if $a(n) = 0$, the conductivity is σ_0.

To test the noise hardness we added a Gaussian noise to the observation signal. One can easily see the bad effect of the noise on the inversion process (see Figure 6), even with a signal to noise ratio of 30 dB. It perfectly illustrates the amplification of the noise by inversion of the smaller eigen values of the direct model.

To overcome this problem, and since we are only considering the simulation cases, we can test here the effect of a regularization process, such as the Wiener regularization [ref]. This inversion is written now:

$$\tilde{A} = [(M^t.M + \sigma_b^{\,2} / \sigma_x^{\,2})^{-1} M^t].OBS \qquad (10)$$

It is interesting to see that, substituting $OBS = M.A$ in the previous equation, we obtain a relation between the real image *A* and the estimated image $\tilde{A}$:

$$\tilde{A} = [(M^t.M + \sigma_b^{\,2} / \sigma_x^{\,2})^{-1}.M^t.M].A \qquad (11)$$

The term between brackets represents the effect of the regularization. The following images (Figures 7 to 8) show the positive effect of this regularization operator, compared to the drastic inversion results without the regularization process.

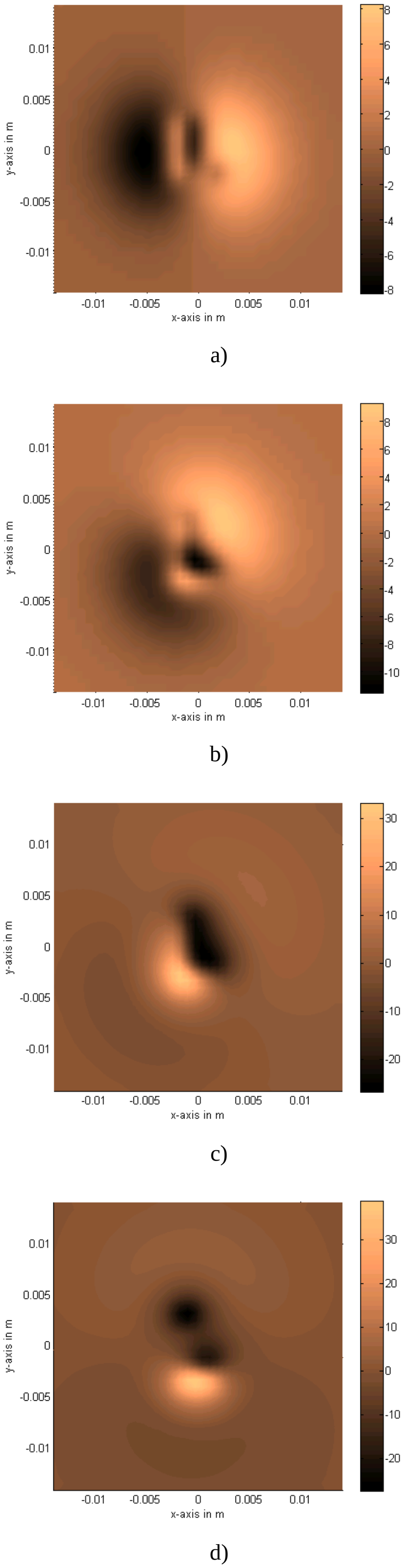

Figure 4 – Examples of images obtained with an 'L' shaped crack

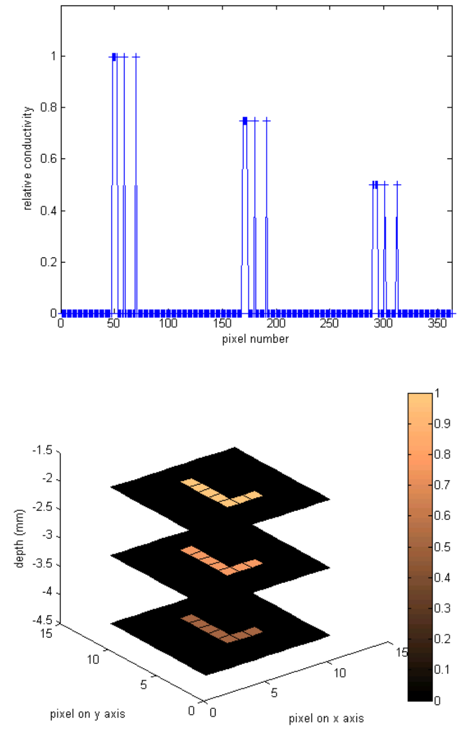

Figure 5 – Reconstructed object without noise: reconstructed image is identical to true object – note that pixels are same as voxels.

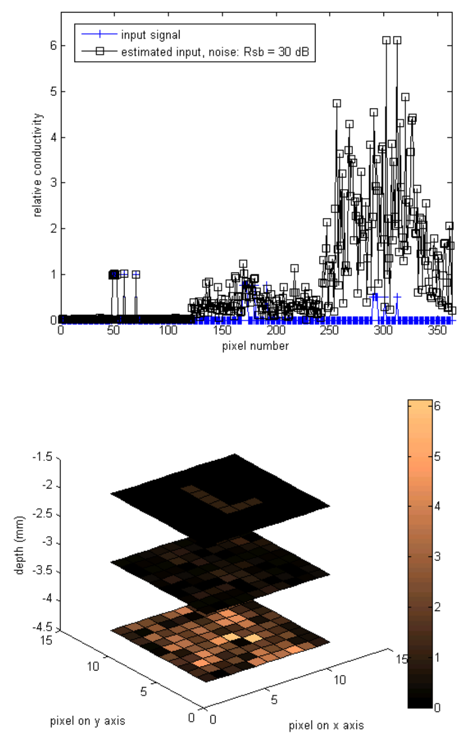

Figure 6 – Reconstruction with least mean squares inversion

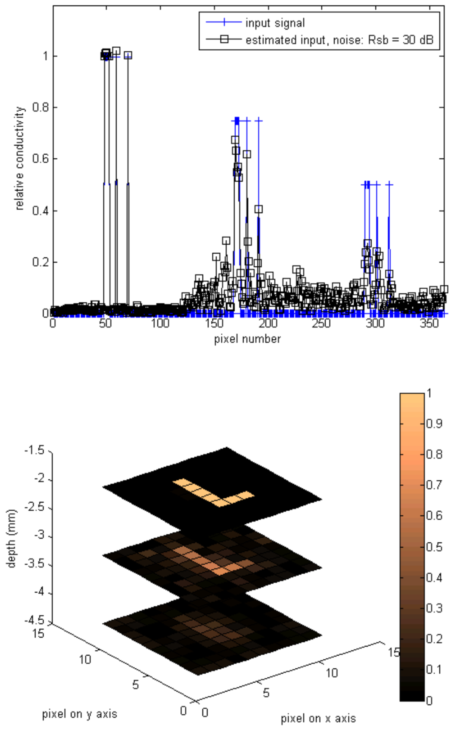

Figure 7 – Reconstruction with Wiener regularization, Rsb=30 dB

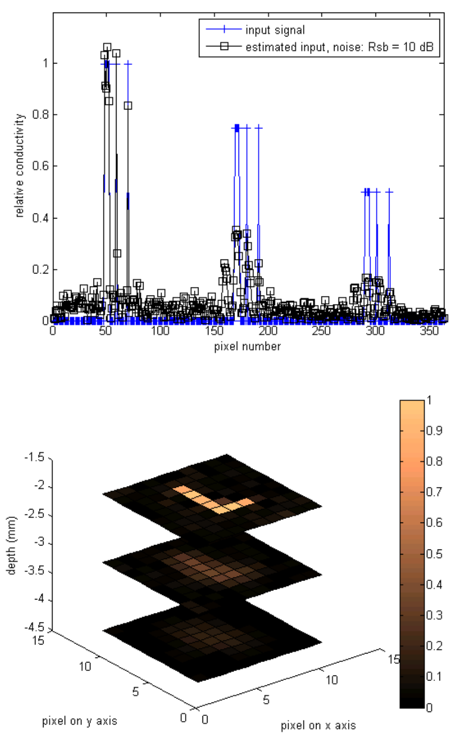

Figure 8 – Reconstruction with Wiener regularization, Rsb=10 dB

4.2 Tomography: Inversion process with an 'imported image'

In the previous case, inversions were performed with the same matrix *M* used for direct image generation and for solving the inverse problem. It was assumed that the defect was built by assembling a given number of different voxels. The resulting image was consequently obtained by superimposing all elemental images (due to a given voxel). In this case, there was no mismatch between the real direct process and the model, because those were identical.

Now, we aims at inverting some 'imported' images obtained by the DPSM model starting from a defect of given shape. We present two examples with one shape of defect: a capsule.

The capsule has has a length of *8.4 mm* and its diameter is *1.2 mm*. Position and dimensions of the capsule are not random; it is chosen to match with the spherical meshing. In this case, the position of the capsule corresponds to the center of the displacement area, in the second layer. We present results in two cases: a capsule oriented along the x-axis and oriented along the y-axis. The first step of the inversion process is to obtain the images of the capsule with our model (the images are not represented here). We need 9 images corresponding to *3* frequencies and *3* inducer orientations. The figure 9 represents some images obtained with the capsule oriented along the x-axis. The figure 9.a was computed for a coil oriented at θ *=0°* and a frequency equal to f_2, the figure 9.b with a coil oriented at θ *=45°* and a frequency equal to f_2, the figure 9.c with a coil oriented at θ *=45°* and a frequency equal to f_3 and the figure 9.d with a coil oriented at θ *=90°* and a frequency equal to f_3.

Once all images are computed, we can build the vector *OBS* :

$$OBS = \begin{pmatrix} \begin{bmatrix} H_z(f_1,\theta=0°) \\ H_z(f_2,\theta=0°) \\ H_z(f_3,\theta=0°) \end{bmatrix} \\ \begin{bmatrix} H_z(f_1,\theta=45°) \\ H_z(f_2,\theta=45°) \\ H_z(f_3,\theta=45°) \end{bmatrix} \\ \begin{bmatrix} H_z(f_1,\theta=90°) \\ H_z(f_2,\theta=90°) \\ H_z(f_3,\theta=90°) \end{bmatrix} \end{pmatrix} \qquad (12)$$

Then, using Equation 10, we can compute the vector $\tilde{A}$.

Figure 10 shows the results of our inversion process, in the case where the object is perfectly estimated for the capsule oriented along the x-axis.

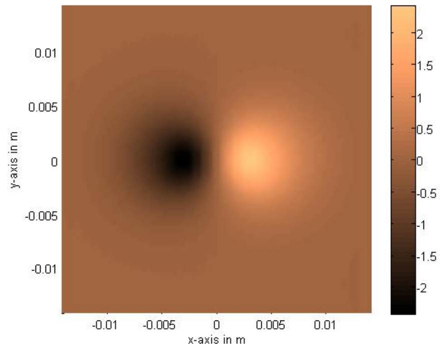

a)

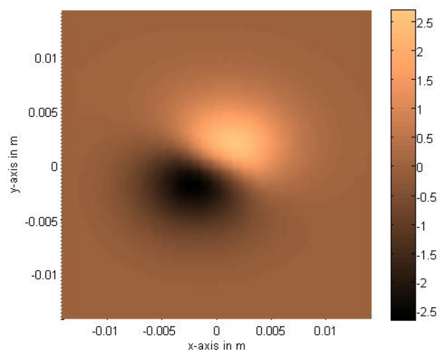

b)

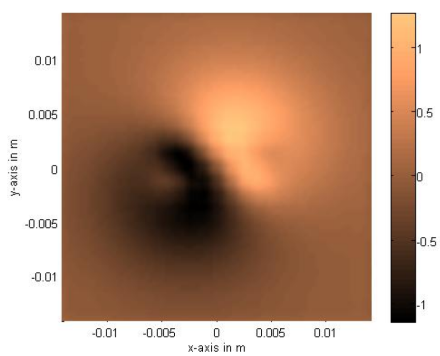

c)

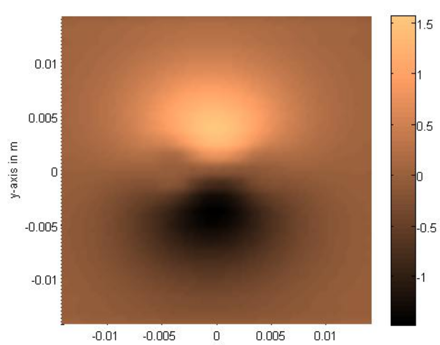

d)

Figure 9 – Examples of images obtained with the capsule oriented along the x-axis

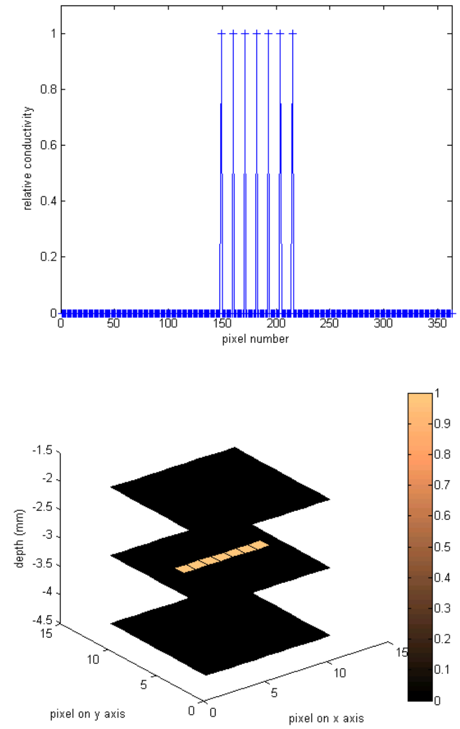

Figure 10 – True values of the relative conductivity of the crack along the x-axis

Figure 11 shows the current reconstruction with Wiener regularization. The difficulty here is to have a good estimate of the noise, for applying equation 10. Remember that this noise can be considered representative of both additive instrumentation noise and model-instrumental mismatch. Here we obtain a satisfying result for Rsb= 15 dB.

Figure 12 represents the results of our inversion process, in the case where the object is perfectly estimated for the capsule oriented along the y-axis; figure 13 shows the current reconstruction with Wiener regularization. A satisfying result is obtained for Rsb= 20 dB.

5. CONCLUSIONS

The results presented in this paper concern the Electromagnetic Modelling of 3D problems for applications in Eddy current crack imaging. The DPSM technique is developed at Ecole Normale Supérieure of Cachan since about ten years, essentially for modelling Electromagnetic problems, and has been briefly presented in this chapter. The reader interested in more details will find such information in some of the references [14]. Because of its relevance and small computation time, this model could be easily used to solve complex problems in quantitative non-destructive evaluation, as done here.

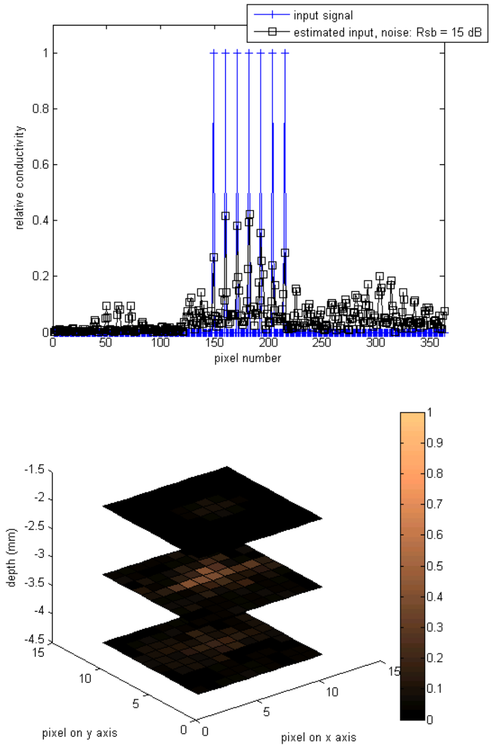

Figure 11 – Reconstruction of the crack along the x-axis with Wiener regularization

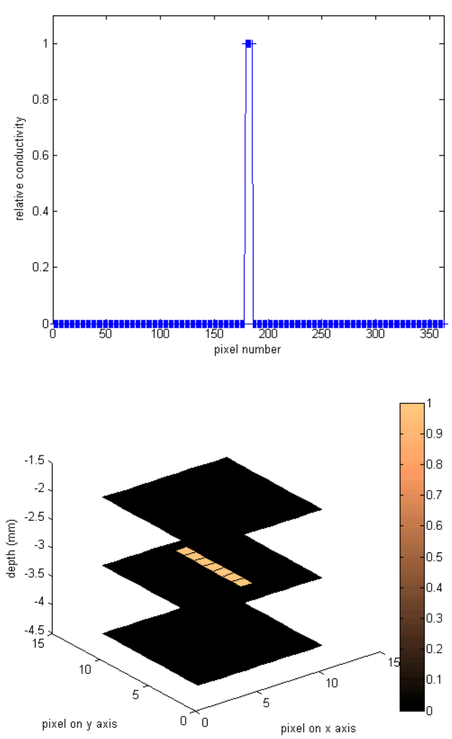

Figure 12 – True values of the relative conductivity of the crack along the y-axis

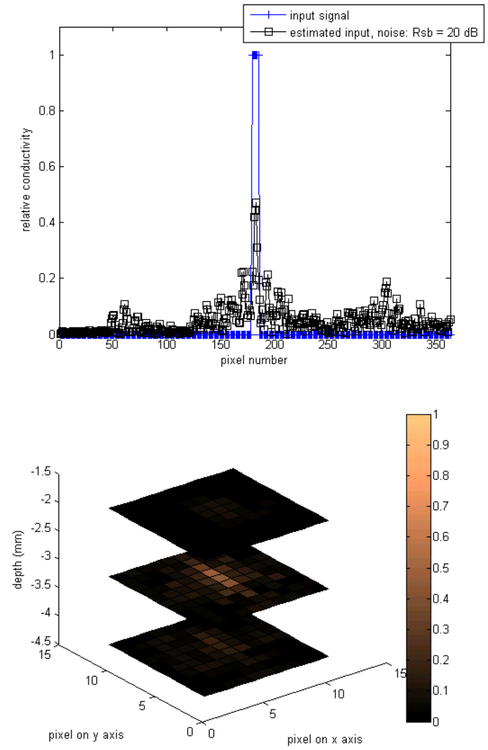

Figure 13 – Reconstruction of the crack along the y-axis with Wiener regularization

Moreover, the SATIE Laboratory has more than 20 years of experience in non destructive testing, with numerous researches and applications concerning industrial problems such as crack detection in steam generators of nuclear power plants, crack detection in aeronautics, and general material property evaluation without contact (non-contact sensor systems).

Our fruitful collaboration with the University of Arizona has also given interesting applications and developments of the DPSM method in Ultrasonic, increasing the generic aspect of the DPSM global method, now applicable in many fields since the Green's functions describing the physical equations in a given medium are well known.

One of the originality of DPSM, concerns the interface modelling, through upper and lower arrays of bubbles containing Equivalent Sources Densities (ESD) disposed on each side of the interface. These source strengths are computed in order to satisfy the boundary conditions, equated at a given array of test points located on the interfaces (or bounding surfaces). In addition, these Equivalent Sources Densities, which are placed inside elemental source volumes (bubbles for example), can be chosen among a large number of possibilities, (elemental points sources, linear or volume density). The simplest model of ESD is obtained with only one point source in each bubble, and is illustrated in the case of Electrostatic sensors, where scalar potential is used. A more complex case containing triplets was illustrated here in Electromagnetic case, where vector potential are necessarily used. The distributed Equivalent Sources Densities lead to a great mathematical simplification of the initial physical problem, which can be then solved through a semi analytical formulation. Good results were obtained, even for a simple kind of Equivalent

Sources Densities (elemental sources points), in different complex domains of Physics (Electromagnetism, Electrostatics, Ultrasonics) which validates the concept presented in this chapter.

Good estimated images of cracks was obtained, even with low signal to noise ratios, showing the interest and robustness of our inversion process. The first step will consist to apply this inversion algorithm to the images obtained with the Eddy Current Imager. Some first results had been obtained, and this process is currently under patent application [15].

6. REFERENCES

[1] Decitre, J.-M.; Premel, D.; Mangenet, G.; Juliac, E.; Feist, W.D.: Flexible EC Array Probe for the Inspection of Complex Parts developed within the European VERDICT Project. In*: Proceedings of 9th ECNDT*, Berlin, 2006, paper Tu.4.4.3.

[2] Dolabdjian C, Wache G, Perez L. Improvement in the detection of subsurface fatigue cracks under airframe fasteners using improved rotating giant magneto-resistance magnetometer head. Insight 2007;49(3):133–6.

[3] Mooke G, Michel F, Simonin J. Electronic imaging using probe arrays. In*: Proceedings of 7th World conference on nondestructive testing*, Shangai, China, 2008.

[4] P. Novotny, P. Saddl, P Machac., A magneto-optic imager for NDT applications, NDT&E Int, 37(8), 2004, 645–649.

[5] Office of Aviation Research, Development of an improved magneto optic/eddy current imager, final report DOT/FAA/AR-97/37, Washington DC, 1998, 20591.

[6] P-Y. Joubert ; Y. Le Diraison and J. Pinassaud. EC imaging device and process for the caracterisation of burried defect in aeronautical structures. Patent n° FR0604255 (2006)

[7] P-Y. Joubert and J. Pinassaud, Linear Magneto-Optic Imager for non-destructive Evaluation.Sensors and actuators A (129) 2006 pp. 126-130.

[8] Le Diraison, Y.; Joubert P.-Y. and Placko, D. 2009. Characterization of Subsurface Defects in Aeronautical Riveted Lap-Joints using Multi-frequency Eddy Current Imaging. *NDT & E International.,* Volume 42, Issue 2, pp 133-140.

[9] Placko D. and N. Liebaux. 2001. Modèle à sources réparties : un concept pour le calcul du champ émis par les circuits magnétiques ouverts. In *Acte du deuxième Colloque Interdisciplinaire en Instrumentation (C2I), Editions Hermès,* pp 523 – 530.

[10] Placko, D. and T. Kundu. 2004. *Chapter 2: Modeling of Ultrasonic Field by Distributed Point Source Method*, in Ultrasonic Nondestructive Evaluation: Engineering and Biological Material Characterization, Ed. T. Kundu, Pub. CRC Press, pp.143-202

[11] Placko, D., T. Kundu, N. Liebaux and A. Cruau, *Procédé universel de modélisation des interactions entre au moins une onde et au moins un objet, la surface de chaque objet définissant une interface entre au moins deux milieux.* French patent N° FR2895544B1, 23/12/05.

Patent Application Canada N° CA2634903A1, 20/12/06.

Patent Application Japon N° JP2008-546450A1, 20/12/06.

Patent Application USA N° US2010-0010781A1, 20/12/06

[12] Placko, D. and T. Kundu. 2007, DPSM for Modeling Engineering Problems, Pub. Wiley.

[13] Coulomb, F. 1984. *Théorie et traitement des signaux, Traité d'électricité, d'électronique et d'électrotechnique,* Ecole Polytechnique Fédérale de Lausanne, Editions Dunod

[14] D. Placko, T. Bore and T. Kundu.. Chapter 4: Distributed Point Source Method for Modelling and Imaging in Electrostatic and Electromagnetic Problems, in Ultrasonic & Electromagnetic NDE for Structure and Material Characterization - Engineering & Biomedical Applications, Ed. T. Kundu, Pub. CRC Press (Tayolor and Francis) (forecast publishing 2012)

[15] Placko, D, Joubert P.-Y and Rivollet A.. Estimation quantitative de défauts présents dans des structures à partir de mesures de grandeurs de surface.

French patent application N° FR10.50514, ENS Cachan/CNRS, 26 January 2010.

International Patent application PCT, 26 January 2011